A high performance contra-rotating energy harvester and its wireless sensing application toward green and maintain free vehicle monitoring

Zhixia Wang [1,2 †], Hongzhi Du [1 †], Wei Wang [1,2*], Qichang Zhang [1,2], Fengshou Gu [3], Andrew D. Ball [3], Cheng Liu [1], Xuanbo Jiao [1], Hongyun Qiu [1], Dawei Shi [3]

[1] *School of Mechanical Engineering, Tianjin University, Tianjin 300350, China*

[2] *Tianjin Key Laboratory of Nonlinear Dynamics and Control, Tianjin 300350, China*

[3] *School of Computing and Engineering, University of Huddersfield, Huddersfield HD1 3DH, UK*

[*] Corresponding author: wwang@tju.edu.cn (Wei Wang)

[†] These authors contributed equally and should be considered co-first authors.

Abstract. Intelligent transportation necessitates advanced perception and cognitive systems that can provide continuous feedback from the vehicle. However, sensors relying on batteries face challenges such as high maintenance costs and environmental issues due to the limited lifespan of the power source. To overcome these challenges, this paper reports an efficient battery-free solution for transportation monitoring. The solution utilizes a speed-amplified rotary energy harvester (SAREH) to power various wireless Bluetooth sensors, enabling continuous monitoring of the vehicle's motion state. The SAREH combines a contra-rotating mechanism with a friction pendulum, resulting in excellent power output in a compact design. Experimental results demonstrate the ability of SAREH to extract power from vehicles operating at speeds ranging from 180 to 1260 rpm. The maximum power output and corresponding power density are measured as 712 mW and 34 mW cm^{-3}, respectively. The prototype successfully powers portable electronics and supports battery-free navigation, triaxial acceleration, and temperature multi-sensors during real road and railway simulation tests. Additionally, the SAREH operates as a highly sensitive speed sensor and an early-warning system for detecting the vehicle's motion state. These results represent a

significant advancement in intelligent transportation systems by showcasing the practicality of self-powered wireless monitoring capabilities on vehicles.

Keywords: Contra-rotating mechanism, Friction pendulum, Energy harvesting, Wireless sensing, Intelligent transportation

1. Introduction

Benefiting from the development of Internet of Things (IoT) devices and smart wireless sensors, transportation can be managed intelligently to enhance safety, convenience, and efficiency [1-3]. Intelligent transportation systems capable of providing various signals, such as vehicle-to-vehicle communication, vehicle monitoring, road warning, and navigation, are gradually entering commercialization and permeating our lives. However, these systems face significant power source challenges [4-7]. Generally, batteries as power sources require extensive upkeep and replacement, causing elevated maintenance costs and environmental problems [8]. On the other hand, traditional cables might be inappropriate due to the messy wiring arrangement, extra weight, and high cost associated with the increasing number of sensors [9]. Moreover, rotational sensors need conductive slip transfers electricity to address the winding issues. Furthermore, embedded sensors make wiring virtually impossible [10]. Thus, searching for a sustainable, portable, and low-carbon power source is necessary, which not only tackles the energy crisis and greenhouse effect but also avoids the entanglement problem.

Energy harvesting is a promising technology to maintain intelligent transportation systems [11], applying various mechanisms including electromagnetic [12-14], piezoelectric [15-17], and triboelectric [18-20] to capture unused and wasted energy around the transports and convert it into renewable electricity [21]. Moving vehicles offer multiple sources of energy for harvesting, such as vehicle mechanical energy,

vehicle-road energy, and wind energy [13, 22-27]. Among them, mechanical energy possesses incomparable advantages: high energy density, low environmental impact, and predictable availability, which make it an attractive and reliable energy source [28, 29].

Extensive efforts have been conducted to develop mechanical energy harvesting structures for intelligent vehicles [30-32]. However, the current state-of-the-art harvesting devices used in land vehicles (trains, automobiles, bicycles), water vehicles (marines), and air vehicles (airplanes) exhibit low energy density in the range of 0.064 μW cm^{-3} to 3.07 mW cm^{-3} (Table S1 of the Supporting Information) [6, 9, 12, 13, 18, 23, 26, 33-38]. Simultaneously, most of these apparatus suffer from bulky size, split design, and inadequate power in low-frequency mechanical energy. As a result, integrating energy harvesting with multiple wireless sensors in a confined space at low frequencies has not yet been reported. Apart from that, gathering real-time signals from rotational parts is still a technical bottleneck due to the time-varying direction field and unsustainable power source [39, 40].

In this work, we present a novel approach to achieve self-powered monitoring for vehicles through the integration of a speed-amplified rotary energy harvester (SAREH) with sensors such as a rotor acceleration sensor, temperature sensor, and GPS sensor. The contributions of the SAREH are as follows: (a) The anchorless mounted contra-rotating transmission amplifies the relative speed of the generation unit to improve conversion efficiency and direct current output power (up to 33 mW cm^{-3}). (b) The

SAREH powers multiple daily appliances and commercial wireless Bluetooth sensors in both laboratory and field settings. (c) As a highly sensitive speed sensor and an early-warning sensor, the device is capable of monitoring the motion state of the vehicle. Therefore, it is believed that the presented work presents an effective wireless monitoring approach for vehicles and supports intelligent transportation systems, as illustrated in Fig. 1.

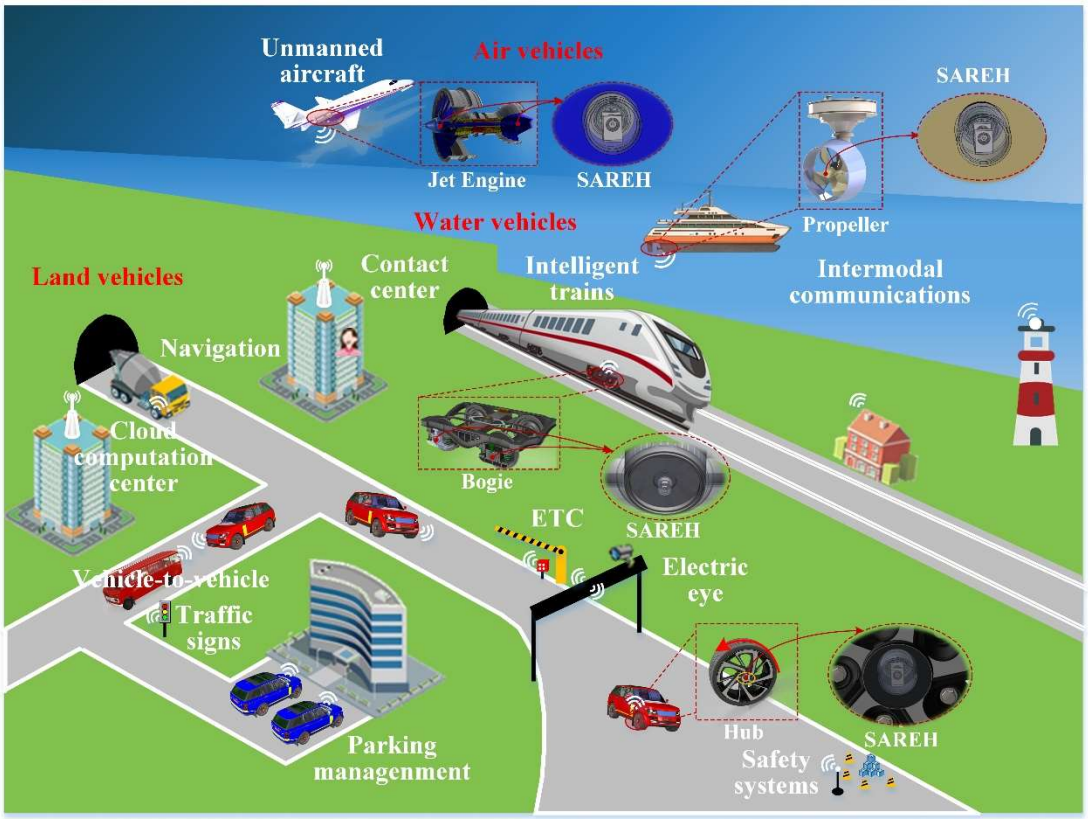

Fig. 1. The SAREH device designed for intelligent transportation systems, consisting of land vehicles, water vehicles, and air vehicles.

2. Design and working principle

Inspired by the design of contra-rotating propellers, the proposed SAREH features a speed amplification design, as illustrated in Fig. 2. The SAREH is composed of five units: a generation unit, a transmission unit, a counterweight unit, a circuit, and a case.

The generation unit incorporates Halbach arrayed NdFeB magnets, three-phase coils, and permeability material. The coils are embedded inside the magnets with permeability material, ensuring a compact size while keeping the coils in the magnetic field. According to Faraday's law, the generation unit produces a voltage when the coils experience a changing magnetic field (Fig. S1 of the Supporting Information). The transmission unit consists of an inner shaft, an outer sleeve, a substrate, three bevel gears, and matched bearings. The inner shaft couples the coils, while the outer sleeve connects the magnets. The gear-bearing not only keeps the coils and magnets rotating in reverse to increase the relative speed between them and thus improve the voltage of the coils but also enhances the stability of the SAREH due to the countervailed rotational moments resulting from the contra-rotating motion. The counterweight unit contributes to the operation of the transmission unit under anchorless mounting conditions. The circuit converts alternating current (AC) to direct current (DC), stores the stable DC, and powers the multi-sensors. The case prevents the generation, transmission, counterweight, and circuit from external interference. From the digital picture (Fig. 2a), it is evident that the prototyped SAREH boasts a small volume as an advantage.

The working principle of the SAREH is as follows: (1) external excitation drives the inner shaft integrated with coils rotates together; (2) the transmission between the inner shaft and outer sleeve causes the outer sleeve, equipped with magnets, to rotate in the opposite direction; (3) the relative motion between the magnets and coils

generates current in the coils. Therefore, the kinetic energy of the vehicle guarantees the synchronous motion of the coils, which then drives the inverse rotation of the magnets via the anchorless transmission, ultimately transducing the energy into electrical energy for powering wireless sensors, as described in Fig. 2b.

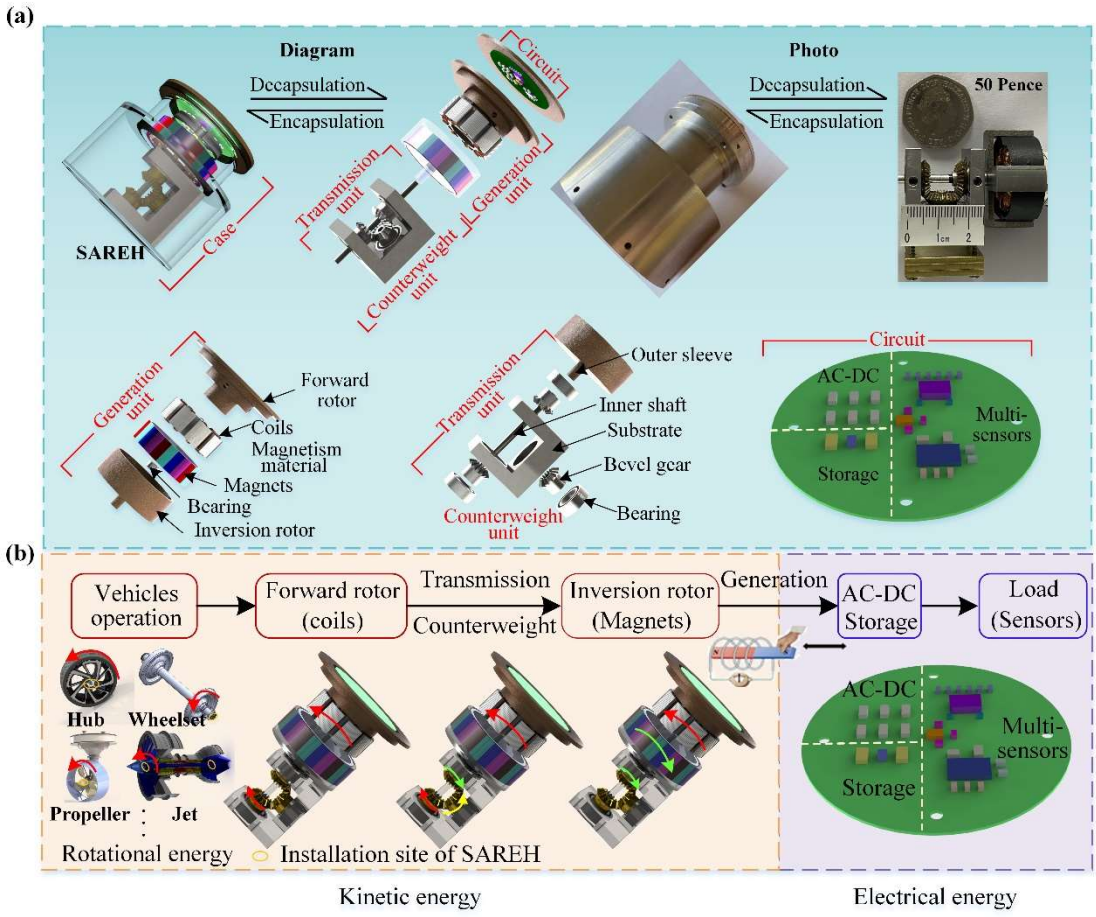

Fig. 2. Design and working principle of the SAREH. (a) Diagram and digital picture of the SAREH, consisting of a generation unit, a transmission unit, a counterweight unit, a circuit, and a case. (b) The energy flows of the SAREH integrated with multi-sensors.

3. Modeling and dynamic analysis of the SAREH

3.1 Modelling of the induced voltage

Based on Faraday's law, the contra-rotation between the coils and magnets results in an induced current due to the variation of magnetic flux passing through the coils.

Therefore, it is necessary to obtain the magnetic flux density produced by the magnets. Fig. 3a demonstrates the arrangement of the magnets with the magnetic direction indicated by an arrow. As displayed in Fig. 3b, the arc magnets can be divided into limited cubic magnets, and the magnetic flux density in point P (r, θ, z) is [41]

$$\begin{aligned} B_r(r,\theta,z)&=\sum_{k=1}^{8}\frac{\varepsilon_k}{4\pi}\sqrt{\ln(-d_y+d)^2+\ln(-d_x+d)^2} \\ B_\theta(r,\theta,z)&=\sum_{k=1}^{8}\frac{\varepsilon_k}{4\pi}\ln(-d_x+d) \\ B_z(r,\theta,z)&=\sum_{k=1}^{8}\frac{\varepsilon_k}{4\pi}\arctan(\frac{d_x d_y}{d_z d}) \end{aligned} \tag{1}$$

where d_x, d_y, d_z, and d are $r\cos\theta$-$r_k\cos\theta_k$, $r\sin\theta$-$r_k\sin\theta_k$, z-z_k, and $\sqrt{d_x^{\,2}+d_y^{\,2}+d_z^{\,2}}$, respectively. ε_k is magnetization of magnet, which alternates signs for positive and negative. Considering all magnets obtains the magnetic flux density of the point P (r, θ, z)

$$\begin{aligned} B_{tr}(r,\theta,z)&=\sum_{i=1}^{n}\sum_{j=1}^{m}B_r(r,\theta,z) \\ B_{t\theta}(r,\theta,z)&=\sum_{i=1}^{n}\sum_{j=1}^{m}B_\theta(r,\theta,z) \\ B_{tz}(r,\theta,z)&=\sum_{i=1}^{n}\sum_{j=1}^{m}B_z(r,\theta,z) \end{aligned} \tag{2}$$

where m is the number of cubic magnets divided by an arc magnet and n is the total number of arc magnets. The coils are perpendicular to the surface of the magnets, then the magnetic flux in the r direction can be calculated by

$$\Phi(t)=\int B_{tr}(r,\theta(t)+\theta_0,z)ds \tag{3}$$

Thus, the induced voltage of the coil is

$$U_i(t) = -N_c \frac{d\Phi(t)}{dt} = -N_c \frac{d\Phi(t)}{d\theta(t)} \frac{d\theta(t)}{dt} = -N_c(2\Omega - \dot{\varphi}) \frac{d\Phi(t)}{d\theta(t)} \tag{4}$$

where N_c represents the number of turns in the coils, Ω denotes the external speed, φ is the pendulum angular, and θ is the relative displacement between the coils and magnets. From the Equation (4) we can conclude that the output voltage is proportional to the relative speed between the magnets and coils, the number of coil turns, and the magnetic flux gradient. Given that the relative speed between the coils and magnets in the speed-amplified rotary energy harvester is about twice that of traditional ones, the output performance of the SAREH is better than the traditional structure without a contra-rotating mechanism. The output power of the load resistance is

$$P = \left(\frac{U}{R_c + R_L} \right)^2 R_L = \left(\frac{N_c(2\Omega - \dot{\varphi}) d\Phi(t)}{(R_c + R_L) d\theta(t)} \right)^2 R_L \tag{5}$$

The maximal output power can be obtained when the external load resistance R_L is equal to the internal resistance of coils

$$P_{max} = = \frac{1}{R_L} \left(\frac{N_c(2\Omega - \dot{\varphi}) d\Phi(t)}{2 d\theta(t)} \right)^2 \tag{6}$$

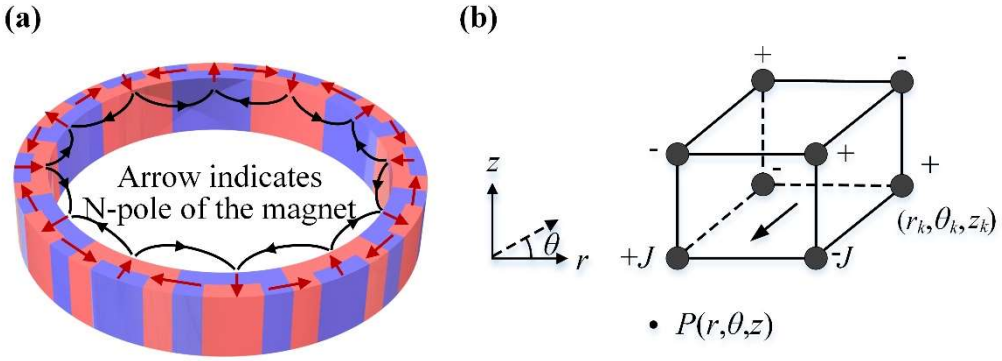

Fig. 3. Design of the magnets. (a) The arrangement of the Halbach arrayed magnets. (b) Modelling magnetic flux density of one cubic magnet.

3.2 Friction pendulum modeling

To calculate the induced voltage, we performed a dynamic analysis on the counterweight. The counterweight, coupled with the bearing pedestal, can be simplified as a friction pendulum around the inner shaft, as shown in Fig. 4a. The pendulum undergoes a cycle of attachment and detachment, indicating alternating static and sliding friction. In stage 1, the pendulum rotates with the inner shaft due to the static friction and magnetic torque, until the gravity torque equals the external torque. In stage 2, static friction transforms into sliding friction, which decreases the friction torque and leads to a reverse rotation. The governing equation for the pendulum is given by

$$J\ddot{\varphi} + m_e gl \sin\varphi = M \tag{7}$$

where m_e is the equivalent mass of the pendulum, and l is the length from the pendulum barycenter to the inner shaft. The external torque M is assumed as

$$M = M_f + M_m = \sum_{i=0}^{2} c_i (\Omega - \dot{\varphi})^i = c_0 + c_1(\Omega - \dot{\varphi}) + c_2(\Omega - \dot{\varphi})^2 \tag{8}$$

where M_f and M_m are friction and magnetic torque, respectively. The damping coefficients c_0, c_1, and c_2 are identified with the external torque M and relative speed $\Omega - \dot{\varphi}$.

The external torque M was measured at different speed by a digital force gauge. The prototype was deployed on a rotational platform and driven by a servo motor, while the counterweight was attached to a force gauge, as shown in Fig. S2a of the Supporting Information. It is important to note that the contact position of the counterweight was

set to the lowest gravitational potential energy. The detailed process is as follows: (1) the prototype's speed was gradually increased from 180 to 1260 rpm in 60 rpm increments, and the maximum/minimum force was recorded at each speed; (2) the above procedure was repeated 5 times to obtain the average force F_a at the same speed to reduce random error; (3) the external torque M was acquired with the average force F_a and pendulum length l.

Similarly, the relative speed was obtained with experiments as depicted in Fig. S2b of the Supporting Information. A laser displacement sensor was positioned at the center of the friction pendulum to measure displacement when the external speed varied from 180 to 1260 rpm with an interval of 60 rpm. This procedure was repeated 5 times to reduce random error and to derive the amplitude and frequency at different speeds, which were subsequently used to calculate the rotational speed $\dot{\varphi}$.

With the assistance of Equation (8), we determined the damping coefficients c_0, c_1, and c_2 to be 1.374 N mm, -0.007946 N mm HZ^{-1}, and 0.002141 N mm HZ^{-2}, respectively, based on the experimental relative speed $\Omega - \dot{\varphi}$, and external torque M. As shown in Fig. 4b, the external torque predicted by Equation (8) agrees well with the experimental data. The external torque gradually increases with the relative speed due to the growth of magnetic torque. The pendulum operates smoothly until the external torque exceeds the maximum gravity torque, and the pendulum occurs in synchronous motion with the inner shaft.

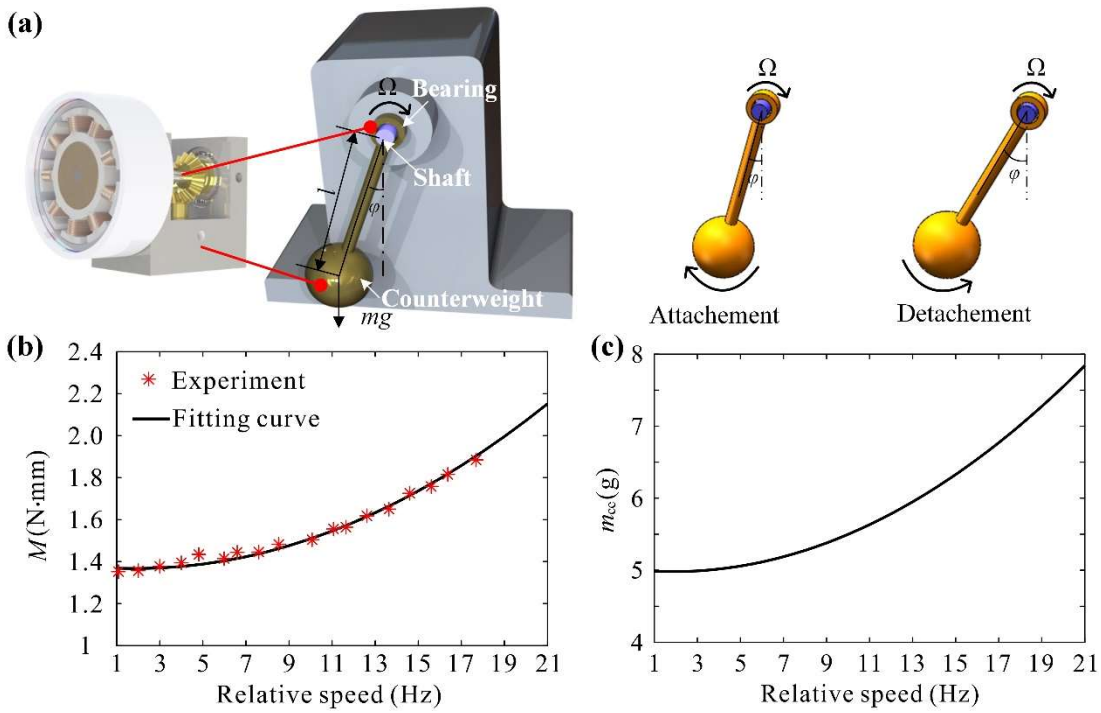

Fig. 4. Friction pendulum modeling and results. (a) The simplified dynamic model of the pendulum. (b) The external torque versus relative speed via experiments and theory. (c) The critical mass of the counterweight under different relative speeds.

The pendulum works perfectly until the gravity torque cannot balance the external torque. When the displacement reaches π/2, the maximum gravity torque is

$$M_{\text{gmax}} = m_{\text{e}} g l \tag{9}$$

The energy accumulation makes the counterweight get over π and eventually rotate with the shaft, thereby defining the corresponding counterweight as the critical mass. When the counterweight mass of the friction pendulum is less than the critical value, the magnets and coils rotate synchronously, causing the harvester to fail. At the critical mass m_{ce}, the external and gravity torque satisfies

$$m_{\text{ce}} g l = c_0 + c_1(\Omega - \dot{\varphi}) + c_2(\Omega - \dot{\varphi})^2 \tag{10}$$

Thanks to Equation (10), we acquired the critical mass of the counterweight under

different relative speeds, as shown in Fig. 4c. For instance, at 2 Hz, the counterweight mass should be above 4.98 g to guarantee the efficient operation of the friction pendulum. Notably, the critical mass increases with the relative speed owing to the enhanced magnetic torque. That is to say, at high speeds, the pendulum experiences a greater external torque and thus necessitates a larger gravity torque to counterbalance the external torque.

The vibration characteristics of the pendulum are related to the output performance of the SAREH from Equation (4). Due to the combined action of the external torque and the gravity torque, the pendulum oscillates around the vibration center at speeds from 180 to 1260 rpm as shown in Fig 5a. Take 180 rpm as an example, the pendulum rotates with the inner shaft to the vibration center until the gravity torque equals the external torque, at which the pendulum vibrates slightly around the center (Fig. 5b).

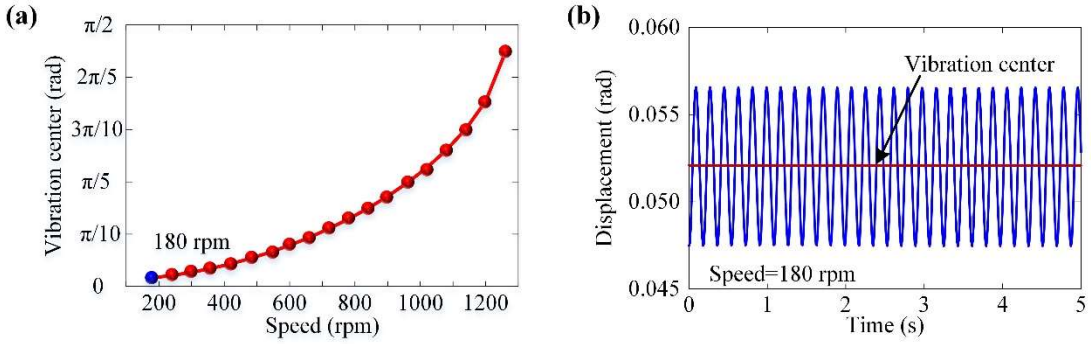

Fig. 5. Vibration characteristic of the friction pendulum. (a) The vibration center of the pendulum under various speeds. (b) The time-displacement curve of the pendulum at 180 rpm.

3.3 Finite-element analysis

To improve the performance of the SAREH, COMSOL Multiphysics® conducts the simulations of magnet arrangement. The AC/DC modules, magnetic field, and

transient state analysis are used in the simulations. The material of the magnets is NdFeB-N35 with a residual flux density of 1.5 T. Comparing the magnetic flux lines distribution of Halbach arrayed and conventionally arrayed magnets (Fig. S3 of the Supporting Information and Fig. 6a), we observed that the Halbach arrayed magnets generated more magnetic flux lines through the coils, covering the entire coil range, which was not the case for conventionally arrayed magnets. Furthermore, the magnetic flux density within the inner (9 mm radius) and the outer (14 mm radius) boundaries of the coils demonstrated that Halbach arrayed magnets produced a more uniform and higher magnetic flux density in coil regions (Fig. S3 of the Supporting Information and Movie S1). This led to a more satisfactory voltage output compared to the conventional arrayed magnets.

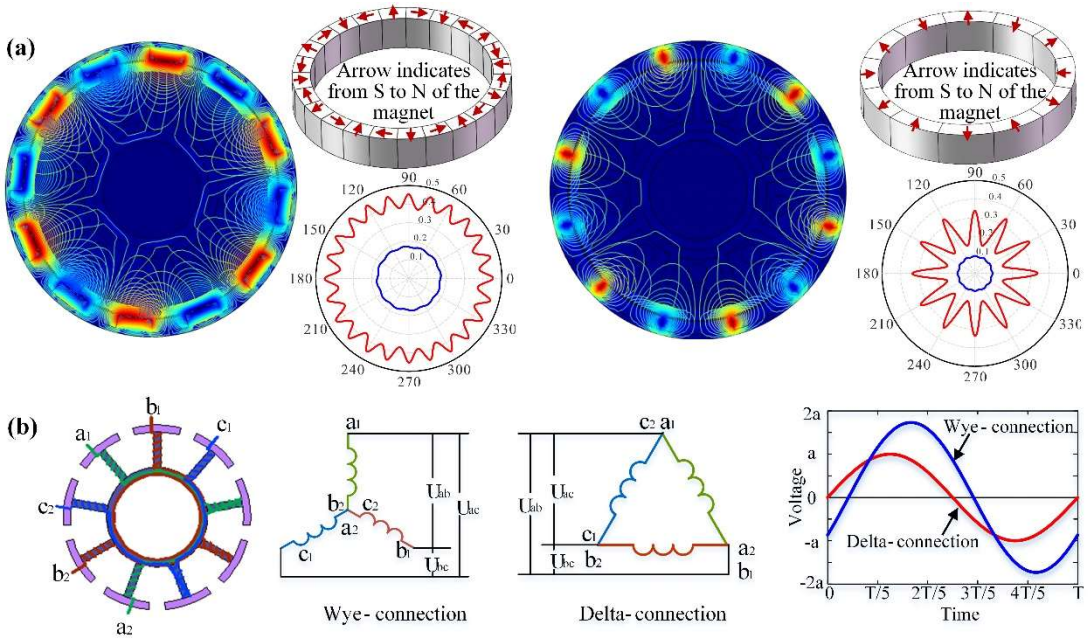

Fig. 6. Finite-element analysis. (a) The layouts of the magnets, magnetic flux line, and magnetic flux density in the inner boundary and the outer boundary of the coils for different layouts of the magnets, the left for Halbach arrayed magnets and the right for conventionally arrayed magnets. (b) The arrangement of the three-phase coils, the

connection of Wye and Delta, and the corresponding output performance.

As presented in Fig. 6b, nine coils are divided into three groups, with the coils in each group connected in series to form a three-phase alternating current. The induced voltages of the three groups are

$$\begin{cases} U_a = A\sin(\omega_g t) \\ U_b = A\sin(\omega_g t - \frac{2}{3}\pi) \\ U_c = A\sin(\omega_g t + \frac{2}{3}\pi) \end{cases} \tag{11}$$

where the amplitude voltage $A = N_c(2\Omega - \dot{\varphi})$, with N_c being the turns of coils; ω_g is the frequency of the induced voltage and can be calculated as [42]

$$\omega_g = N_m(2\Omega - \dot{\varphi})/4 \tag{12}$$

where N_m is the magnetic pole pairs of the Halbach arrayed magnets. The three-phase alternating current connects the external resistance via Wye and Delta connections. Fig. 6b also illustrates the line and phase voltage, and the line voltage of the Wye connection is

$$\begin{cases} U_{ab} = U_a - U_b = \sqrt{3}A\sin(\omega_g t - \frac{2}{3}\pi) \\ U_{ac} = U_a - U_c = \sqrt{3}A\sin(\omega_g t + \frac{2}{3}\pi) \\ U_{bc} = U_b - U_c = \sqrt{3}A\sin(\omega_g t) \end{cases} \tag{13}$$

Based on the Delta connection, the voltage across each coil is the same as the phase voltage. However, in the Wye connection, the voltage across each coil is $\sqrt{3}$ times that of the Delta connection. Hence, we chose to use the Wye connection for the proposed harvester.

Given that magnetic pole pairs influence the magnetic field distribution of the Halbach array, we simulated magnetic flux density with phase and magnetic pole pairs. The results demonstrate that the increased pole pair improves the radial and tangential magnetic flux density, and the waveform period of magnetic flux density increases with the increase of the magnetic pole pair as shown in Fig. 7a. Nevertheless, the increased magnetic pole pair aggravates the difficulty of processing and installation of magnets. Therefore, the Halbach array with 6 magnetic pole pairs prototypes the SAREH. From Figure 7b, we can conclude that the thickness of the magnet has little effect on the radial and tangential flux density. Considering the installation space and coil size, the height of the magnet is set to 10 mm.

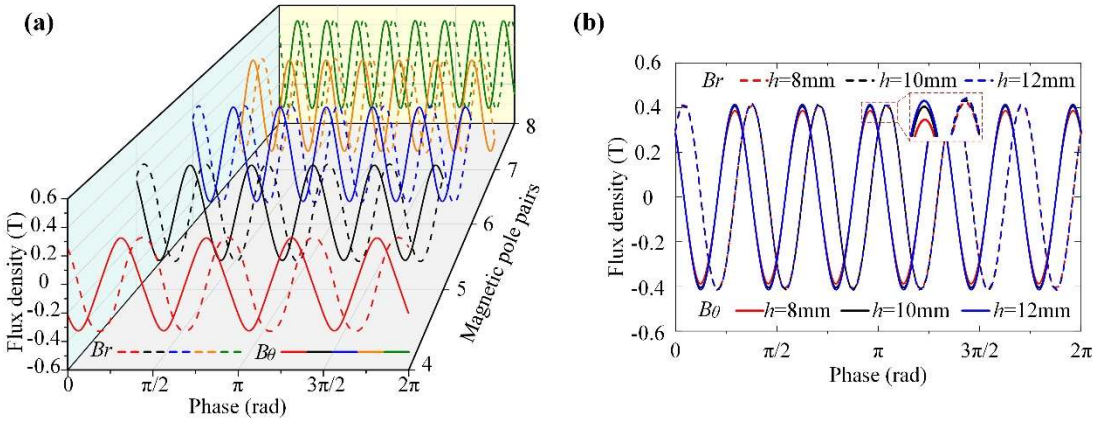

Fig. 7. The radial and tangential magnetic flux density at the outer (14 mm radius) boundaries of the coils with 10 mm height of the Halbach array magnets. (a) Magnetic pole pairs and (b) magnetic height.

4. Performance investigation

4.1 Prototype fabrication and experimental setup

Generation unit: A hollow foundation with a 3 mm inner diameter, 9.7 mm outer diameter, and 5 mm height is made of aluminum, and three-phase coils were mounted

on its outer diameter. It is essential to note that the diameter of the coils is 0.1 mm and the number of turns in each phase is 500 turns. A ring magnet with dimensions of R15×14×10 mm, composed of 6 groups of Halbach arrayed magnets, is wrapped in an aluminum film and fixed on a base to prevent magnetic leakage and resist electromagnetic interference. An up sleeve with a 682ZZ deep groove ball bearing is embedded to ensure relative motion between the shaft and the magnet case, and a down sleeve is used to hold the transmission unit. The dimensions of the case sleeve, up sleeve, and down sleeve are R17×15×14 mm, R3.5×2.5×4 mm, and R1.5×1×5 mm, respectively. Transmission unit: A U-shaped bearing pedestal was deployed in the counterweight case, and the three sides were positioned with a through-hole to anchor an MR106ZZ deep groove ball bearing. These bearings guide and provide radial forces for the transmission process, which involves an up bevel gear mounted on the down sleeve of the magnet case, a down bevel gear installed on an R3 mm shaft connected to a hollow foundation, and a side bevel gear that engages with the up and down gears. The bevel gears are made of H59 brass with 15 teeth and 0.5 modules. The size of the transmission unit could be reduced by using smaller bearings and gears. Furthermore, a multiplying ratio cylindrical gear could amplify the relative motion between the coils and the magnets. Counterweight case: The counterweight connects with the bearing seat of the transmission unit. To increase its gravity torque in the limited space, the counterweight is made of H62 brass. It is worth noting that we mounted a case on the coil foundation to encapsulate, protect the interior structure, and form an integrated

device with wireless sensors. The whole volume, weight, and cost of the SAREH are about 21.2 mm^3, 86.46 g, and 12.57 USD, respectively. The material properties and structural parameters of the proposed SAREH as shown in Table S2 of the Supporting Information.

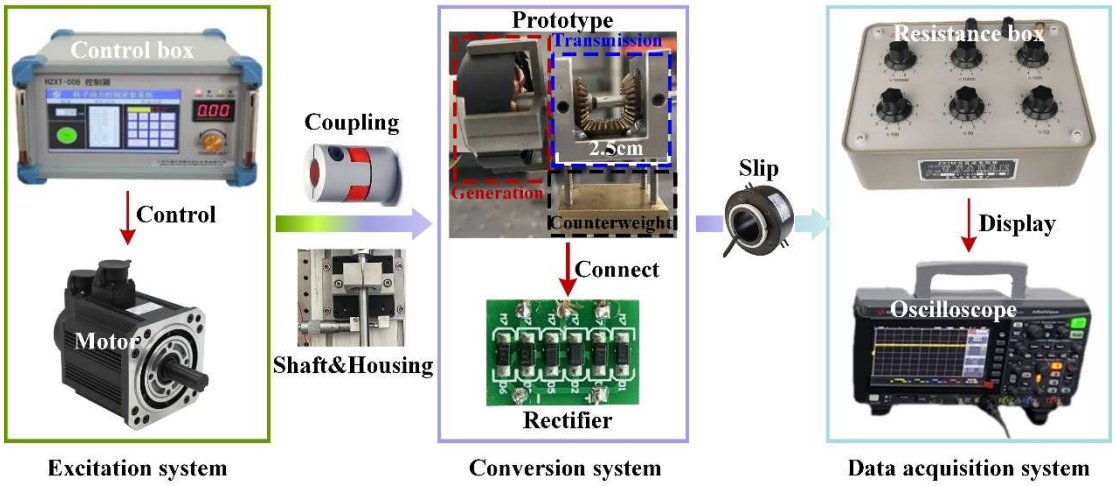

Fig. 8. Experimental setup for testing characteristics and the enlarged view of the SAREH and its corresponding rectifier.

Experiments were conducted to evaluate the performance of SAREH as shown in Fig. 8. The prototype was excited by a speed-controlled servo motor (model: HZXT-008, Wuxi Houde Automation Meter CO., LTD.). A rectifier through a slip ring (model: 1500 rpm high-speed slip ring, Senring) exported the three-phase voltage. The output voltage across a resistance box (model: ZX1M, DoMore) was measured with an oscilloscope (model: DSOX1204G, Keysight) to determine the optimal resistance of the proposed harvester. The alignment of the SAREH and the servo motor was ensured by the micrometer of the bearing base and the gaskets of the motor base and housing base. Additionally, the motor shaft was rigidly connected to the foundation hollow of

the generation unit using a sleeve.

4.2 Electrical output characteristics of the prototyped energy harvester

Ensuring excellent electrical output of the harvester is crucial for wireless sensors in vehicles. Therefore, we investigated the performance of the SAREH, as shown in Fig. 9a-e. To observe the motion of the counterweight, the case of the SAREH was removed during the experiments. According to the typical vehicle speeds (Table S3 of the Supporting Information), we explored the RMS voltage responses of the harvester in the range of 180 - 1260 rpm. The average voltage increases proportionally with the speed (Fig. 9a), revealing that the vehicle speed can be identified from the voltage. Therefore, the SAREH is capable of detecting the real-time speed and improving the operation safety factor of vehicles. The stable DC voltage signals in the SAREH's output domain confirm its sensitivity as a speed sensor (Fig. S4a of the Supporting Information). Additionally, the harvester stores the stable DC output in capacitors to provide continuous electricity for low-power devices.

In addition, considering that the counterweight may flip π, leading to synchronous rotation between the coils and magnets and a sharp drop in output voltage for emergency braking, abnormal vibration, or passing speed bumps of vehicles, the SAREH served as an early-warning sensor to assess motion state and improve the reliability of vehicles. We simulated the anomalous vibrations of vehicles by perturbing SAREH, and the resulting output signal is shown in Fig. 9b. The output signal maintained around 9.5 V at 504 rpm before the counterweight climbed π and the storage

capacitor voltage dropped to 2.5 V after 80 s.

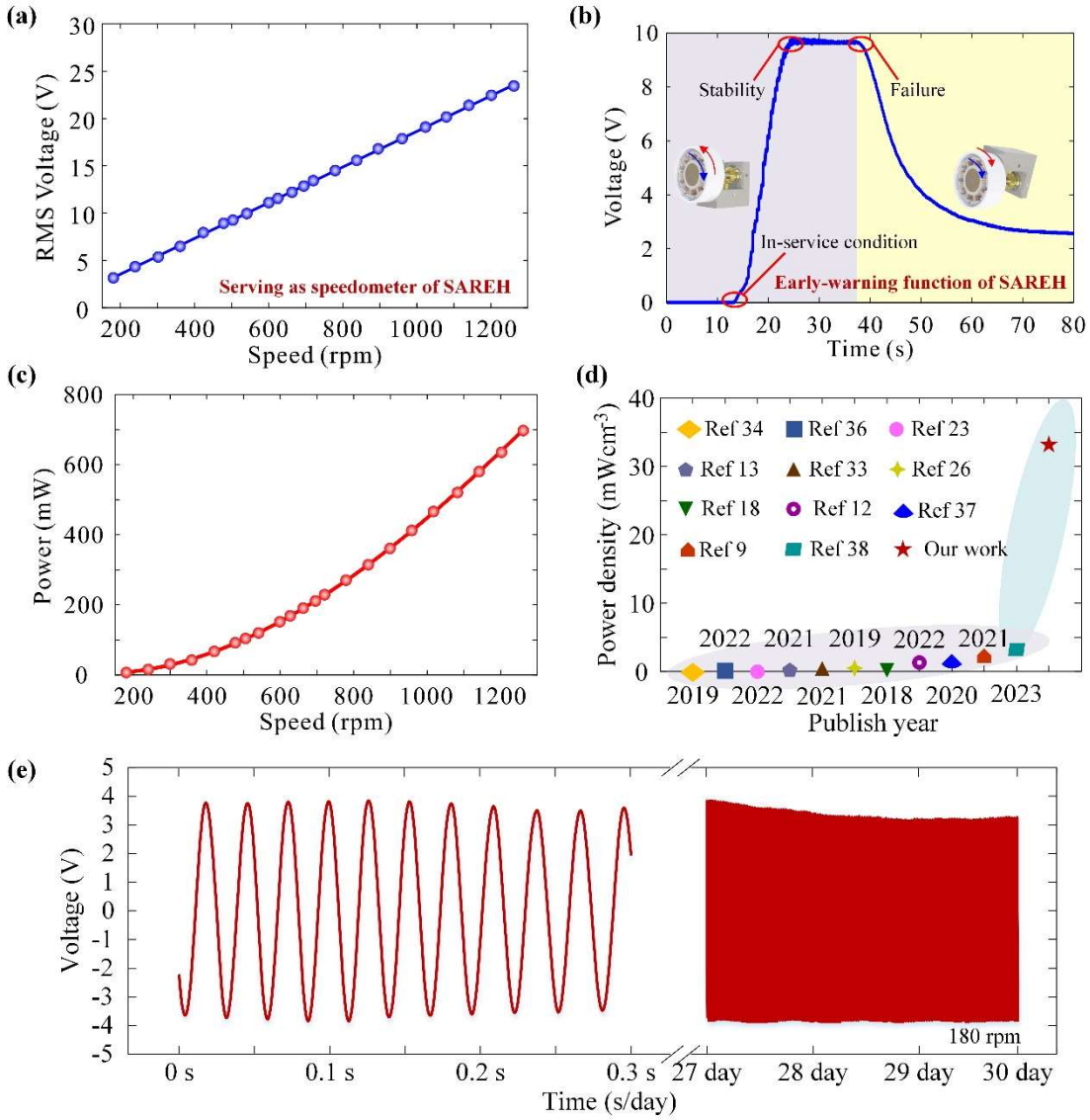

Fig. 9. Electrical output characteristics of the prototyped energy harvester. (a) The prototype serves as a speedometer and (b) an early-warning sensor for vehicles. (c) The output power versus various external speeds with optimal resistance. (d) Comparison of the SAREH with recently reported vehicle harvesters. (e) The output stability and mechanical durability of the SAREH.

To characterize the capability performance, we examined the power output with a variation of the connected resistance at different speeds (Fig. 9c). In the experiments, the proposed harvester was connected to a resistance box, where the resistance varied

from 10 to 500 Ω with the step of 10 Ω and 100 Ω in the range of 10 - 300 Ω and 300 - 500 Ω, respectively. The output voltage and power versus resistance at typical frequencies indicate that the prototype achieved a maximum power under a matched resistance of 160 Ω at different speeds (Fig. S4b of the Supporting Information). While the output voltage across the resistance increased rapidly and quickly became saturated. The maximum average power reached 8.9 - 712 mW with optimal resistance at 180 - 1260 rpm, the corresponding highest power density being 33.74 mW cm^{-3}. To verify the theoretical results, we compare the experimental and theoretical open-circuit output voltage of the SAREH. The theoretical results are in good agreement with the experimental results (Fig. S5 of the Supporting Information).

The comparison (Fig. 9d, Fig. S6 and Table S4 of the Supporting Information) between the SAREH and recently reported vehicle energy harvester illustrates that the proposed harvester produces an excellent stable DC power density due to the speed amplification mechanism, Halbach arrayed magnets, and the limited volume. In fact, the output power of the harvester is positively correlated with the volume. The SAREH has a smaller volume, so it has a rather lower output power compared to other reported results. Owing to the small volume, harvesters can be symmetrically installed on the axle box or embedded in the axle of the wheelset to improve output power without impacting the operation of vehicles. Besides, employing gears such as solar and planetary gears further increases the relative speed of the magnets and coils to optimize the performance of the SAREH. Furthermore, the durability of the SAREH is a crucial

index to check for commercial applications, so we carried out a durability test on a 1/1-scale wheelset at a speed of 180 rpm at CRRC Tangshan Co., LTD. Based on the maintenance cycle of the freights, the durability of the SAREH was evaluated in a month. In the experiment, the open-circuit voltage is a directly measured parameter that can evaluate the output characteristics of the prototype. Therefore, the durability of the SAREH was tested by comparing its output voltage after 30 days of its initial use, as shown in Fig. 9e. The output stability, mechanical durability, and system safety of the prototype satisfy the design requirements of onboard sensors for vehicles.

In Fig. 10, we analyze the influence of the speed amplification mechanism and magnet arrangement on the output performance of the harvester. Given that the frequency and amplitude of the voltage in the three-phase coil are identical (Fig. 10c), to facilitate the comparison of the voltage performance for different harvesters, a group of the coil was selected as the representative. The alternating current of the SAREH increased from 3.72 to 26.22 V with the increase of the rotational speeds from 180 to 1260 rpm (Fig. 10a). Fig. 10b depicts the output voltage of the SAREH without a speed amplification mechanism as the function of the rotational speeds. It can be observed that the speed amplification mechanism improves the output voltage and enhances the operation frequency. The RMS DC voltages under different rotational speeds for SAREH, SAREH without the speed amplification mechanism, and non-speed amplified harvester with conventionally arranged magnets in reference 9 reveal that the combination of the speed amplification mechanism and Halbach arranged magnets

optimizes the output performance of the harvester (Fig. 10d).

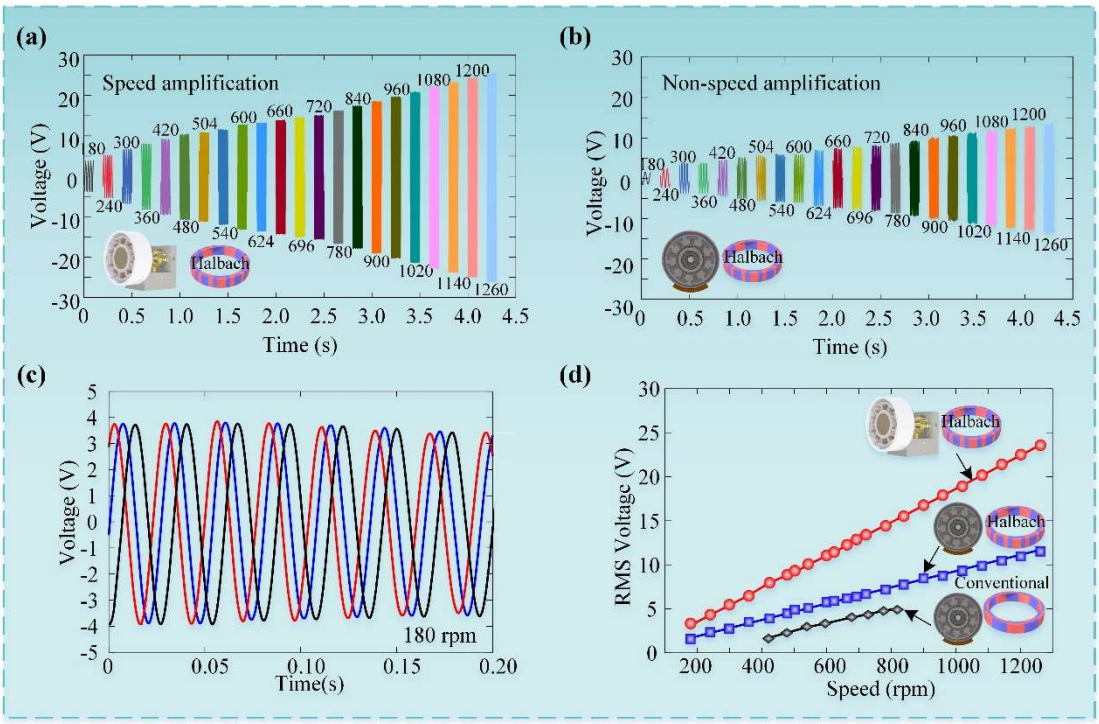

Fig. 10. The output performance of harvester with different structures. The open-circuit AC voltage of the harvester with (a) speed amplification and (b) non-speed amplification with rotational speed ranging from 180 to 1260 rpm. (c) The AC voltage of the three-phase coil in the SAREH at a fixed working speed of 180 rpm. (d) The RMS DC voltage under different rotational speeds for SAREH, SAREH without speed amplification mechanism, and non-speed amplified harvester with conventionally arranged magnets.

To provide power for onboard sensors in freight rail transport and automobile, SAREH can be deployed on the shaft or even embedded in the wheelset shaft, as shown in Fig. 11. For instance, assuming that the operating time of the vehicles is 4 hours, the total power consumption of onboard sensors for trains and automobiles is 8.75 kJ and 2.44 kJ, respectively (Table S5 of the Supporting Information). The prototype SAREH generates 2.85 kJ at a train speed of 250 km h^{-1} and produces 0.84 kJ (Fig. 8c) at 80 km h^{-1} for automobiles. Hence, the developed SAREH meets the power requirements of

onboard sensors, enabling intelligent freight or smart cars. The power of the 3 V 240 mAh button cell used in sensors is 2.59 kJ. The cost of the button cell (Panasonic CR2032) is one-fifteenth of the SAREH. The payback period of the SAREH is about 4 days and 13 days for trains at 250 km h^{-1} and automobiles at 80 km h^{-1} when the univalent energy of the SAREH and button cell is the same.

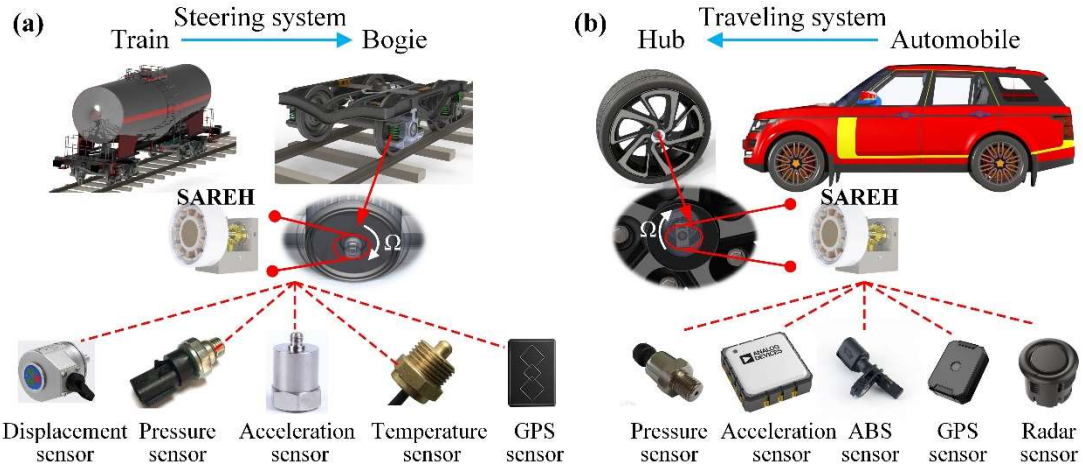

Fig. 11. The prototyped energy harvester as a power source drives common low-power onboard sensors of the land vehicles: (a) the train and (b) the automobile.

4.4 Powering devices and sensors of the harvester in the lab

To verify the potential application of SAREH as a power supply, we connected the rectifier in parallel with a 560 μF capacitor (model: 1210) and zener diodes (model: MCC349B) to ensure a stable DC voltage. Due to its high output voltage, SAREH can simultaneously charge low-power devices through a series resistance at low-speed excitation. The electricity generated by the harvester can be stored in batteries (Fig. 12a), which serves as a sustainable, portable, and low-carbon power source for wireless vehicle sensors. Furthermore, SARAH can power a 5 V LED lamp and maintain portable electronic devices (such as the Huawei P10 cellphone and Honor Band 4

smartwatch) at 280 rpm, as demonstrated in Fig. 12b and Movie S2.

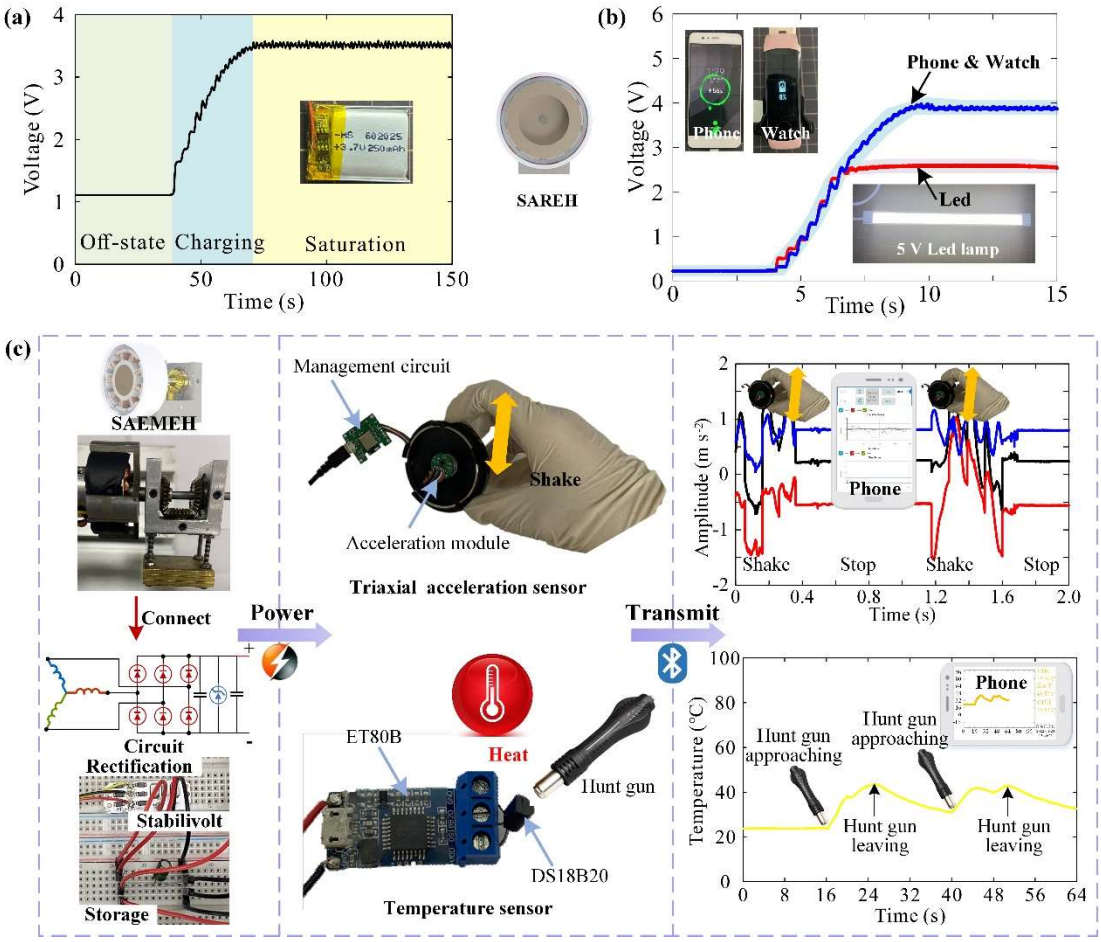

Fig. 12. The application of the SAREH in the lab. (a) Charging a 3.7 V 250 mAh lithium battery. (b) Powering synchronism portable electric devices. (c) Maintaining multiple wireless Bluetooth sensors module to transmit signals.

SAREH integrated with a wireless sensor is capable of providing feedback on the operation conditions of the vehicle. We design a wireless monitoring triaxial on-rotor acceleration sensor to address the problem of rotational objects acceleration wireless monitoring. The on-rotor sensor supports a wide range of accelerations and frequencies, from ±2 g to ±16 g and 500 to 8000 Hz, respectively, to match the characteristics of the measured object. It operates on a direct voltage range of 2.7 V to 5 V and the detailed circuit diagram for the acceleration sensor is shown in Fig. S7 of the Supporting

Information. Since the axis temperature in vehicles is essential, we also synchronized a commercial wireless temperature sensor. The temperature sensor measures temperatures from -55 ℃ to 125 ℃ with a resolution of 0.0625 ℃ and operates on a supply voltage range of 3.5 - 5.5 V. Fig. 12c and Movie S3 demonstrated that the prototype successfully drove the acceleration and temperature sensors to send signals under 350 rpm.

4.5 On-vehicle evaluation of the SAREH

To demonstrate the feasibility, the SAREH integrated with multiple wireless sensors was installed on a wheel hub of Fan-Volkswagen T-ROC (Fig. S8a of the Supporting Information), and the performance was measured on a real road at Tianjin University (Fig. S8b of the Supporting Information). The car traveled approximately 600 m between points A and point B. The round trip A-B-A covered a total distance of more than 20 miles, demonstrating the mechanical durability and output reliability of the harvester.

Since the harvester can support sensors at low rotational speed, the vehicle traveled at low speeds while powering wireless acceleration, temperature, and GPS sensors. With the tire diameter d_{wheel} and rotational speed v_{RPM}, the vehicle speeds can be calculated as

$$v = 0.06\pi d_{\text{wheel}} v_{\text{RPM}} \tag{14}$$

The 215/55R17 tire in the Fan-Volkswagen T-ROC indicates the tire diameter being 66.83 cm. According to the lab experiments, the prototyped harvester was able to

power simultaneously acceleration and temperature sensors under 350 rpm, thereby controlling the vehicle speed around 44 km h^{-1} in real road tests.

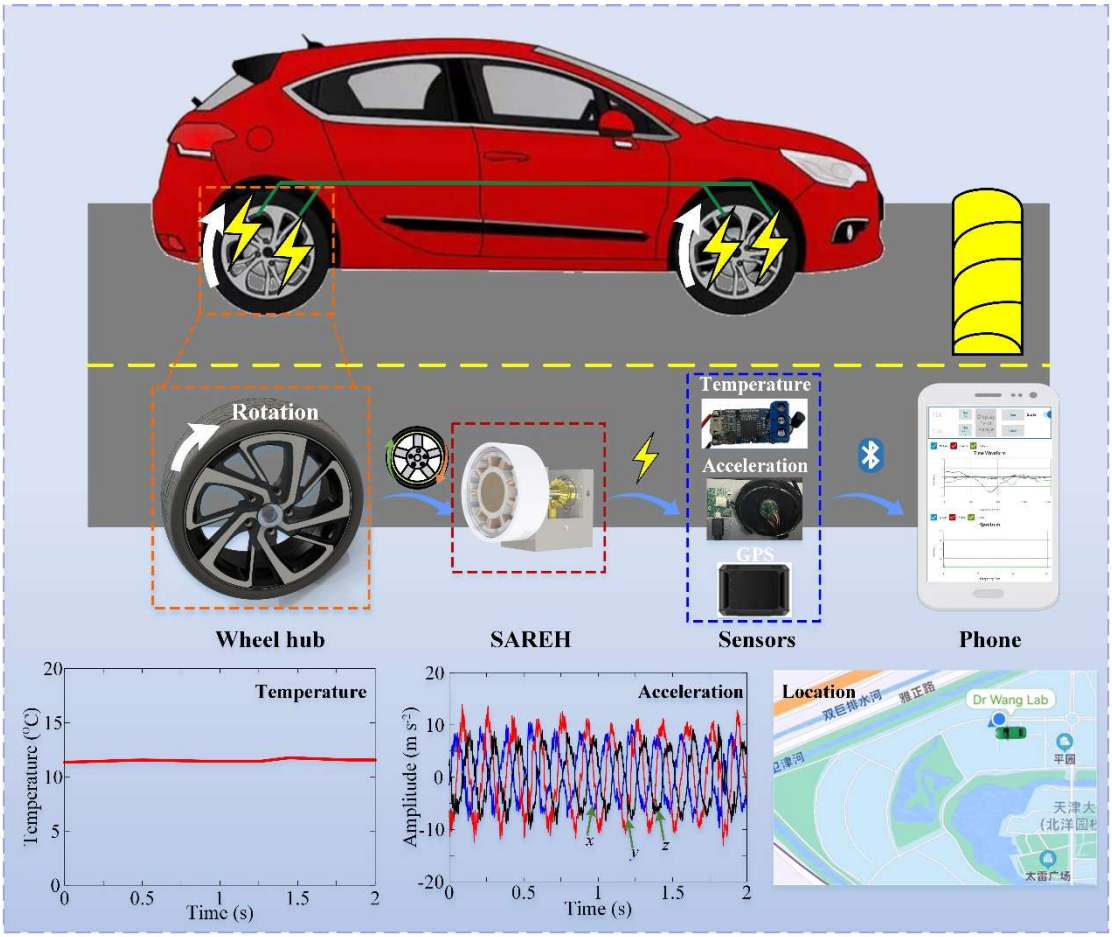

Fig. 12. On-vehicle evaluation of the SAREH. The real-time shaft temperature, acceleration, and vehicle position owing to the prototype integrated with wireless Bluetooth temperature, rotor triaxial acceleration, and GPS sensor in practical road tests.

The SARAH integrated with multiple wireless sensors was capable of monitoring the triaxial acceleration and temperature of the wheel hub in real-time via a mobile phone (Fig. 13 and Movie S4). Additionally, Fig. 13 also illustrates that the SAREH was capable of driving a GPS module to send the position information of the running vehicle (Movie S5). The GPS sensor locates vehicles via the BeiDou navigation satellite system, with intelligent and periodic positioning modes that feedback position

information every 10 seconds and 10 minutes, respectively. The GPS sensor operates on a direct voltage range of 2.7 - 5.5 V.

Fig. 14. Railway evaluation of the SAREH. Self-powered wireless shaft temperature and triaxial acceleration monitoring during the railway simulation tests.

The SAREH effectively captures the rotational motion of the wheelset for generating induced voltage to supply stable electricity to the wireless sensors. Four roller rigs stimulate the rotation of wheelsets in a 1/2-scale freight wagon. A triple-phase asynchronous motor drives the roller rig via a gearbox, and the speed of the motor is adjustable through a control box. The wheel profile of the wheelset, bogie frames, and freight wagons was machined as standard 75 kg m^{-1} metals, K6, C70 in proportion. As a result, the rotational response of the axles in the wheelset is similar to that of a real vehicle. We deployed the SAREH on the wheelset using a 3D-printed connection, bolts, and thread holes in the axles. The rotational speed of the 1/2-scale wheelset was controlled at approximately 250 rpm during the railway simulation tests. Since there are no cables in the freight wagon, the SAREH holds significant value in harnessing

rotational energy for self-powered monitoring of wheelset bearing temperature in railway environments. More importantly, the rotor triaxial acceleration with the SAREH enables the detection and feedback of wheelset derailment conditions in trains, as shown in Fig. 14 and Movie S6.

5. Conclusion

In summary, we developed a battery-free wireless monitoring system with a novel speed-amplified rotary energy harvester. To achieve multiple sensing in confined spaces on the vehicles, we fabricated anchorless transmission and Halbach arrayed magnets for manufacturing the energy harvester. The counterweight acted as the friction pendulum to guarantee operation for contra-rotating transmission under anchorless mounting conditions; in addition, the generation unit achieved contra-rotation, thus improving the output power. The experimental results indicated that the output DC voltage was 3.2 - 23.6 V at 180 - 1260 rpm and the corresponding power was 8.9 - 712 mW with a maximum power density being 33.74 mW cm^{-3}. As for application, the prototype maintained portable electric devices and supported common wireless sensors simultaneously in practical road and railway simulation tests; the SAREH could also serve as a high-sensitivity speed sensor and an early warning sensor to monitor the motion state of vehicles. We believe that our results will pave the path for the next generation of self-powered monitoring for vehicles in intelligent transportation systems.

CRediT authorship contribution statement

Zhixia Wang: Investigation, Conceptualization, Validation, Funding acquisition,

Visualization, Writing - original draft. **Hongzhi Du**: Investigation, Conceptualization, Validation, Visualization. **Wei Wang**: Conceptualization, Supervision, Funding acquisition, Writing - review & editing. **Qichang Zhang**: Supervision, Writing - review & editing. **Fengshou Gu**: Validation, Supervision, Writing - review & editing. **Andrew D. Ball**: Supervision, Writing - review & editing. **Cheng Liu**: Validation. **Xuanbo Jiao**: Data Curation. **Hongyun Qiu**: Investigation. **Dawei Shi**: Software.

Declaration of competing interest

The authors declare that they have no known competing financial interests or personal relationships that could have appeared to influence the work reported in this paper.

Acknowledgments

This work was supported by the National Natural Science Foundation of China (Grant Nos. 12302022, 12172248, 12132010, 12021002), the Tianjin Research Program of Application Foundation and Advanced Technology (Grant No. 22JCQNJC00780), and IoT Standards and Application Key Laboratory of the Ministry of Industry and Information Technology (Grant No. 202306).

Appendix A. Supplementary material

Supplementary material related to this article can be found online.

Data availability

Data will be made available on request.

References

[1] Feng S, Yan X, Sun H, Feng Y, Liu H. Intelligent driving intelligence test for

autonomous vehicles with naturalistic and adversarial environment. Nat Commun 2021; 12.

[2] Askari H, Khajepour A, Khamesee MB, Wang Z. Embedded self-powered sensing systems for smart vehicles and intelligent transportation. Nano Energy 2019; 66: 104103.

[3] Bernal E, Spiryagin M, Cole C. Onboard condition monitoring sensors, systems and techniques for freight railway vehicles: a review. IEEE Sens J 2019; 19: 4-24.

[4] Zhao X, Askari H, Chen J. Nanogenerators for smart cities in the era of 5G and Internet of Things. Joule 2021; 5: 1391-1431.

[5] Lee DG, Shin J, Kim HS, Hur S, Sun S, Jang J, et al. Autonomous resonance-tuning mechanism for environmental adaptive energy harvesting. Adv Sci 2022: 2205179.

[6] Maurya D, Khaleghian S, Sriramdas R, Kumar P, Kishore RA, Kang M, et al. 3D printed graphene-based self-powered strain sensors for smart tires in autonomous vehicles. Nat Commun 2020; 11.

[7] Pang Y, Zhu X, Yu Y, Liu S, Chen Y, Feng Y. Waterbomb-origami inspired triboelectric nanogenerator for smart pavement-integrated traffic monitoring. Nano Res 2022; 15: 5450-5460.

[8] Tan YK. Energy harvesting autonomous sensor systems: design, analysis, and practical implementation. UK London: CRC Press, 2017.

[9] Wang Z, Wang W, Gu F, Wang C, Zhang Q, Feng G, et al. On-rotor electromagnetic energy harvester for powering a wireless condition monitoring system on bogie

frames. Energ Convers Manage 2021; 243: 114413.

[10] Fu H, Mei X, Yurchenko D, Zhou S, Theodossiades S, Nakano K, et al. Rotational energy harvesting for self-powered sensing. Joule 2021; 5: 1074-1118.

[11] Tang X, Wang X, Cattley R, Gu F, Ball A. Energy harvesting technologies for achieving self-powered wireless sensor networks in machine condition monitoring: a review. Sensors-Basel 2018; 18: 4113.

[12] Miao G, Fang S, Wang S, Zhou S. A low-frequency rotational electromagnetic energy harvester using a magnetic plucking mechanism. Appl Energ 2022; 305: 117838.

[13] Wang Y, Li S, Gao M, Ouyang H, He Q, Wang P. Analysis, design and testing of a rolling magnet harvester with diametrical magnetization for train vibration. Appl Energ 2021; 300: 117373.

[14] Pan Y, Lin T, Qian F, Liu C, Yu J, Zuo J, et al. Modeling and field-test of a compact electromagnetic energy harvester for railroad transportation. Appl Energ 2019; 247: 309-321.

[15] Yang Z, Zhou S, Zu J, Inman D. High-performance piezoelectric energy harvesters and their applications. Joule 2018; 2: 642-697.

[16] Wang Z, Wang W, Tang L, Tian R, Wang C, Zhang Q, et al. A piezoelectric energy harvester for freight train condition monitoring system with the hybrid nonlinear mechanism. Mech Syst Signal Pr 2022; 180: 109403.

[17] Mahapatra SD, Mohapatra PC, Aria AI, Christie G, Mishra YK, Hofmann S, et al.

Piezoelectric materials for energy harvesting and sensing applications: roadmap for future smart materials. Adv Sci 2021; 8: 2100864.

[18] Qian J, Kim D, Lee D. On-vehicle triboelectric nanogenerator enabled self-powered sensor for tire pressure monitoring. NANO ENERGY 2018; 49: 126-136.

[19] Miao Y, Gao S, Kong Y, Jiang Z, Han Q, Chu F. Variable reluctance bearing generators applicable in condition monitoring of bearing cages. Mech Syst Signal Pr 2023; 194: 110249.

[20] Zhao H, Xu M, Shu M, An J, Ding W, Liu X, et al. Underwater wireless communication via TENG-generated Maxwell's displacement current. Nat Commun 2022; 13.

[21] Wang C, Ji Y, Lai S, Liu Y, Hao Y, Li G, et al. A speed-amplified tri-stable piezoelectric-electromagnetic-triboelectric hybrid energy harvester for low-frequency applications. Nano Energy 2023; 114: 108630.

[22] Fang Z, Tan X, Liu G, Zhou Z, Pan Y, Ahmed A, et al. A novel vibration energy harvesting system integrated with an inertial pendulum for zero-energy sensor applications in freight trains. Appl Energ 2022; 318: 119197.

[23] Zhao L, Zou H, Zhao Y, Wu Z, Liu F, Wei K, et al. Hybrid energy harvesting for self-powered rotor condition monitoring using maximal utilization strategy in structural space and operation process. Appl Energ 2022; 314: 118983.

[24] Park H, Kim J. Electromagnetic induction energy harvester for high-speed railroad applications. Int J Pr Eng Man-Gt 2016; 3: 41-48.

[25] Gao M, Wang P, Cao Y, Chen R, Cai D. Design and Verification of a Rail-Borne Energy Harvester for Powering Wireless Sensor Networks in the Railway Industry. IEEE T Intell Transp 2017; 18: 1596-1609.

[26] Pan Y, Liu F, Jiang R, Tu Z, Zuo L. Modeling and onboard test of an electromagnetic energy harvester for railway cars. Appl Energ 2019; 250: 568-581.

[27] Zhang B, Chen J, Jin L, Deng W, Zhang L, Zhang H, et al. Rotating-disk-based hybridized electromagnetic-triboelectric nanogenerator for sustainably powering wireless traffic volume sensors. ACS Nano 2016; 10: 6241-6247.

[28] Wang C, Lai S, Wang Z, Wang J, Yang W, Ni Y. A low-frequency, broadband and tri-hybrid energy harvester with septuple-stable nonlinearity-enhanced mechanical frequency up-conversion mechanism for powering portable electronics. Nano Energy 2019; 64: 103943.

[29] Zhang Y, Wang W, Xie J, Lei Y, Cao J, Xu Y, et al. Enhanced variable reluctance energy harvesting for self-powered monitoring. Appl Energ 2022; 321: 119402.

[30] Germer M, Marschner U, Richter A. Energy harvesting for tire pressure monitoring systems from a mechanical energy point of view. IEEE Internet Things 2022; 9: 7700-7714.

[31] Rodrigues C, Nunes D, Clemente D, Mathias N, Correia JM, Rosa-Santos P, et al. Emerging triboelectric nanogenerators for ocean wave energy harvesting: state of the art and future perspectives. Energ Environ Sci 2020; 13: 2657-2683.

[32] Qi L, Pan H, Pan Y, Luo D, Yan J, Zhang B. A review of vibration energy harvesting

in rail transportation field. Iscience 2022; 25: 103849.

[33] Gao M, Cong J, Xiao J, He Q, Li S, Wang Y, et al. Dynamic modeling and experimental investigation of self-powered sensor nodes for freight rail transport. Appl Energ 2020; 257: 113969.

[34] Zhang X, Yu M, Ma Z, Ouyang H, Zou Y, Zhang SL, et al. Self-powered distributed water level sensors based on liquid-solid triboelectric nanogenerators for ship draft detecting. Adv Funct Mater 2019; 29: 1900327.

[35] Wang H, Zhu Q, Ding Z, Li Z, Zheng H, Fu J, et al. A fully-packaged ship-shaped hybrid nanogenerator for blue energy harvesting toward seawater self-desalination and self-powered positioning. Nano Energy 2019; 57: 616-624.

[36] Gao S, Han Q, Jiang Z, Zhang X, Pennacchi P, Chu F. Triboelectric based high-precision self-powering cage skidding sensor and application on main bearing of jet engine. Nano Energy 2022; 99: 107387.

[37] Wang Y, Yang Z, Li P, Cao D, Huang W, Inman DJ. Energy harvesting for jet engine monitoring. Nano Energy 2020; 75: 104853.

[38] Huo S, Wang P, Long H, Ren Z, Yi Q, Dai J, et al. Dual-mode electromagnetic energy harvester by Halbach arrays. Energ Convers Manage 2023; 286: 117038.

[39] Feng G, Hu N, Mones Z, Gu F, Ball AD. An investigation of the orthogonal outputs from an on-rotor MEMS accelerometer for reciprocating compressor condition monitoring. Mech Syst Signal Pr 2016; 76-77: 228-241.

[40] Xu Y, Tang X, Feng G, Wang D, Ashworth C, Gu F, et al. Orthogonal on-rotor

sensing vibrations for condition monitoring of rotating machines. Journal of Dynamics, Monitoring and Diagnostics 2022; 1: 29-36.

[41] Luo A, Zhang Y, Dai X, Wang Y, Xu W, Lu Y, et al. An inertial rotary energy harvester for vibrations at ultra-low frequency with high energy conversion efficiency. Appl Energ 2020; 279: 589-603.

[42] Zhang Y, Cao J, Zhu H, Lei Y. Design, modeling and experimental verification of circular Halbach electromagnetic energy harvesting from bearing motion. Energ Convers Manage 2019; 180: 811-821.